

An experimental study of cellular mechanical interface in a bi-material structure fabricated by material extrusion additive manufacturing

Sumit Paul, Li Yang

Department of Industrial Engineering, University of Louisville, Louisville, USA

Abstract

This work is a continuation of the preliminary project with the investigation of the characteristics of the cellular structure-based mechanical interlocking interface designs for bi-material structures fabricated by material extrusion additive manufacturing (AM). Three different cellular designs, including auxetic, body centered cubic (BCC), and octahedral, were investigated for the topology design effects on the interface performance. In addition, the effects of build orientation and interface polarity were also studied. The results clearly suggested that the cellular-based mechanical interlocking interface exhibit significantly enhanced ductility and energy absorption that can be desirable to many applications, and that the interface characteristics are influenced by both the topology design of the cellular structures and the intrinsic properties of the processed materials.

1. Introduction

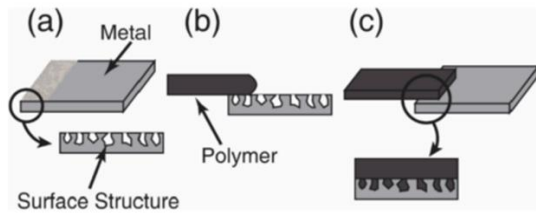
Multi-material with additive manufacturing (AM) is being extensively investigated due to the expanded designability with more than one materials available in the structures. Through the introduction of heterogeneous materials, advanced design concepts such as functionally gradient materials (FGM) or metamaterials can not only have locally optimized architectures for performance requirements, but also achieve higher level of design optimality. On the other hand, the fabrication of multi-material components imposes additional challenge. Various design factors must be considered, such as differences in thermal behaviors of materials, the interfacial integrity, and the interaction of multiple material phases under mechanical and physical loading conditions. Such design framework requires comprehensive consideration of material models, topology designs, as well as the corresponding AM processes, which is currently lacking in general [1].

Various AM processes routinely employ multi-material printing, such as material extrusion, material jetting and sheet lamination. Among them, material extrusion is among the most broadly adopted processes, due to its capability to readily print multiple materials via the configuration of multiple printhead nozzles. Various literatures have reported the use of material extrusion for multi-material structure printing in different applications. Watschke et al. [2] printed ABS-PLA dual material samples by material extrusion and did tensile testing, lap-shear, compression-shear tests. Yang et al. [3] developed a material extrusion 3D printer for continuous fiber reinforced thermoplastic composites. Khondoker et al. [4] proposed a bi-extruder material extrusion multi-material printer for FGMs made from immiscible thermoplastics and tested mechanically interlocked extrudates of PLA, ABS and polystyrene.

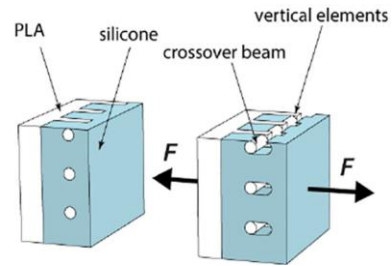
However, the material option for the multi-material printing with material extrusion is in general limited. Freund et al. [5] evaluated the peeling resistance and roll peeling resistance of interfaces between a number of common material pairs using material extrusion, including ABS/NinjaFlex, XT/NinjaFlex, XT-CF20/NinjaFlex, GF30-PA6/NinjaFlex, GF30-PP/NinjaFlex, PLA/NinjaFlex, ABS/TPU-93 and PLA/TPU-93. Results showed that with most combinations the interfacial strength is limited. Similar conclusion was also drawn by Lopes et al. [6]. The limitation with material selection results in design limitations. In many cases, material pairings with significantly different properties (e.g. hydrophobic + hydrophilic, soft + hard) are needed for desired functionality, and in these cases the intrinsic material compatibility could become a significant barrier for the adoption of AM technologies.

One traditionally-established concept that might provide an effective solution to the multi-material compatibility challenge is the mechanical interlocking design. The concept of mechanical interlocking design for multi-component structures utilizes the structural interaction between the components to introduce structural integrity. Instead of diffusion bonding at the material interfaces or fastening, the interactions among the components such as contact and sliding result in coordinated deformation, and therefore the mechanical strength of the interlocking design. Mechanical interlocking design has been extensively employed in certain application areas such as woven fabric structure designs. Another perhaps more popular example is the Chinese wooden puzzles. Therefore, the interlocking design mechanism has the potential to overcome the limitation with intrinsic material compatibility and to achieve adequate interfacial strength.

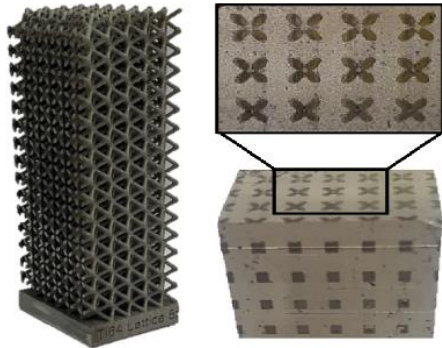
There currently exist some literatures that demonstrate the performance of mechanical interlocking multi-material interface designs. Zhao et al. [7] investigated mechanical interlocking between A5052 aluminum alloy and 30% glass-fiber-reinforced polybutylene terephthalate joined by injection molding the polymer to the pre-treated textured metal surfaces (Fig.1a). It was found that the strength of the interface is determined by both the injection molding process parameters and the topology design of the surface texture. Rossing et al. [8] investigated an interlocking concept based on grid-like scaffold for PLA-silicone multi-material structures (Fig.1b), and the results showed significant improvement of part integrity despite the low intrinsic material interfacial strength between the two materials. Cellular structure design concepts have also been explored, due to their interconnected porosity that inherently accommodates interlocking design. Perets et al. [9] studied the mechanical properties and biocompatibility of a biodegradable implant design with Ti6Al4V cellular structures made by laser powder bed fusion additive manufacturing (L-PBF-AM) and filled with a Mg-based alloy (Fig.1c). Although the study did not focus on the interface design, the design approach resulted in good structural integrity and improved balance of performance. Verma et al. [10] investigated cellular structure-based interlocking design for a 316L stainless steel-AV651 epoxy resin bi-material interface. The cellular structures were designed with several unit cell topologies (BCCZ, CFCC and Kelvin) and manufactured using L-PBF-AM, and subsequently filled with the resin via injection molding (Fig.1d). The results clearly suggested that the properties of the interface are significantly influenced by the selection of the cellular unit cell topology designs.



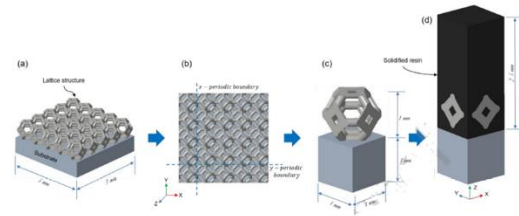
a. Metal-polymer interlocking interface via injection molding over textured surface [7]



b. PLA-silicone interface via crossover beam-based interlocking design [3.1]



c. Ti6Al4V-Mg multi-material design with cellular scaffold [9]



d. 316L Stainless steel-AV651 resin interlocking design with cellular scaffold [10]

Fig.1: Mechanical interlocking designs from literature

In this study, three types of cellular unit cell designs, including octahedral, re-entrant auxetic, and BCC, were investigated for the cellular-based mechanical interlocking designs for the PLA-PETG bi-material interface. The two materials were chosen due to the expectation of low compatibility as well as material availability at the time of the study. This was also a continuation of the preliminary study that was previously reported [11]. The three types of unit cells were chosen in the attempt to investigate potential significance of representative design rules. The octahedral structure is a stretching-dominated design and exhibits directional isotropy. The re-entrant auxetic structure exhibits negative Poisson's ratio and is a bending dominated design. The BCC structure is a bending-dominated design and exhibits positive Poisson's ratios (Fig.2). An experimental study was carried out for the mechanical property evaluation of interfaces based on the three unit cell designs, and the results were also compared to additional finite element analysis (FEA) for insights into the structural behaviors.

2. Materials and Methods

2.1. Design of experiment

In this study, relative density of the cellular design was the only geometry design parameter that was investigated. To minimize the effect of other geometry parameters, the geometry aspect ratio of each of the unit cell designs was arbitrarily decided and kept constant, and the design of relative density was achieved by isotropic scaling of the unit cell dimensions. In addition, the strut thickness of each type of unit cells was also kept constant at all levels of relative densities. Fig.2 shows the unit cell designs, and Table 1 lists the geometry designs of all three types of unit cell structures in

order to achieve the three levels relative density (0.3, 0.4 and 0.5), as well as the relative density levels. The relative density levels were determined based on the reference material strength of PLA and PETg from literature, which were set to be about 18MPa and 12MPa, respectively [6, 7].

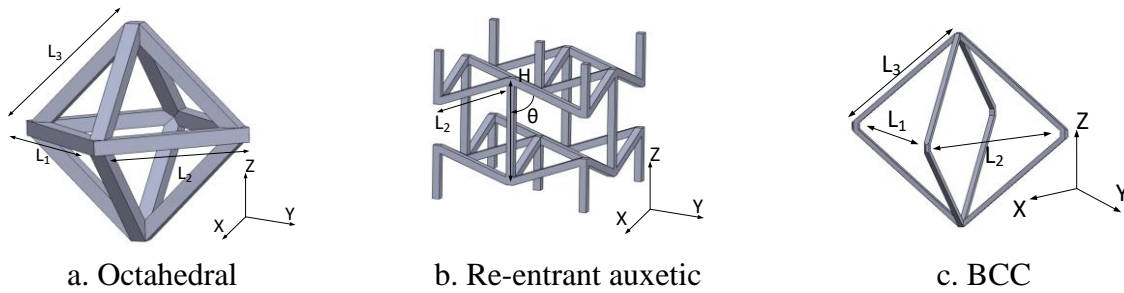


Fig.2 Unit cell design for the cellular structures

Unit cell	Relative density (Design/Actual)	L_1/H (mm)	L_2 (mm)	L_3 (mm)	θ (deg)	t (mm)
Re-entrant auxetic	0.4/0.397	3.9	2.97		75	1.3
	0.5/0.509	3.3	2.51		75	1.3
	0.6/0.608	2.9	2.2		75	1.3
BCC	0.4/0.395	7.63	7.63	6		1.9
	0.5/0.505	6.48	6.48	5.1		1.9
	0.6/0.602	5.72	5.72	4.5		1.9
Octahedral	0.4/0.399	4.3	4.3	4.3		1.3
	0.5/0.506	3.6	3.6	3.6		1.3
	0.6/0.560	3.3	3.3	3.3		1.3

Table 1: Design parameters of the cellular lattice structures (positive component)

For the interface design, the cellular structures constructed by the unit cell designs (Fig.2) were conveniently termed “positive” component, which were then filled with their complementary geometries that were termed “negative” component, as shown in Fig.3. The interfaces were designed into the shape of tensile testing coupons, albeit not following the dimension guidance of ASTM E8.

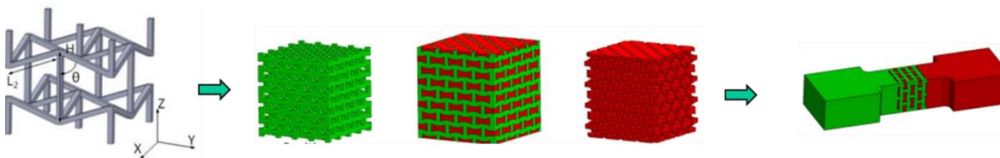


Fig.3 Design of the interface samples

In order to establish comprehensive design of experiment (DOE) space, designs with material assignment of both PLA and PETg to the positive component were included in the investigation. Consequently, the naming of the sample designs follow the custom of “unit cell design”-“relative density (RD) level”-“positive material”, i.e. Aux-40RD-PETg means that the baseline cellular design is an re-entrant auxetic with a 0.4 relative density, and the material for the positive

component is PETg. Following such DOE, a total of 18 design combinations were included in the study. Due to the resource limitation, 2-3 samples were fabricated for each design.

In addition, in order to establish the baseline mechanical properties for the intrinsic material interface, both single-material tensile coupons and bi-material planar interface samples were designs. As shown in Fig.4, bi-material tensile coupon models with the two components overlapping (shown as d in Fig.4) by 0mm, 0.1mm, 0.5mm, 0.7mm and 1mm were designed and fabricated.

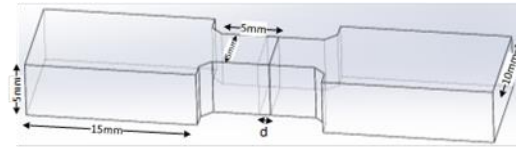


Fig.4 Benchmark interfacial strength evaluation sample design

2.2.Sample fabrication

The samples were fabricated using a FlashForge Creator Pro 3 material extrusion printer. A preliminary process development study was carried out before the fabrication of the actual samples, in order to ensure adequate material affinity that avoids component detachment during the printing. Such process was done in an ad-hoc way without the concern of achieving truly optimized process settings, therefore is not reported in this paper. Afterwards, the parameters were fixed for all the samples. **Table 2** lists the process parameter settings used for printing the samples, and Fig.5 illustrates the fabricated samples (Re-entrant auxetic with 0.4 relative density). All the cellular interface design samples as well as the single-material tensile coupons were fabricated successfully. On the other hand, the benchmark bi-material tensile coupons with 0mm and 0.1mm interface overlap completely failed to maintain part integrity. The rest of the benchmark coupons were fabricated successfully.

Process parameter	Setting	Process parameter	Setting
Layer height (mm)	0.30mm	PLA nozzle temperature (°C)	195
Substrate temperature (°C)	70	PETG nozzle temperature (°C)	225
Base printing speed (mm/s)	60	Travel speed (mm/s)	100
# of shells (shell layers) @all sides	2	Maximum perimeter path overlap (%)	30
Infill pattern	Line	Infill (%)	100
Infill cross angle (°)	90	Infill start angle (°)	45
Use of brim	None		

Table 2: Process parameter values



a. Aux-40RD-PLA: PLA (black) in positive component



b. Aux-40RD-PETg: PETg (grey) in positive component

Fig.5 Fabricated samples: Re-entrant auxetic with 0.4 relative density

The samples were subjected to standard tensile testing using an Instron 5569A universal tensile tester with a 5KN load cell. The displacement of the crosshead was utilized for the calculation of elastic modulus, which was expected to introduce some error. However, due to the low elastic modulus with the structures, this error was not considered significant enough to create biased observations and therefore not further addressed.

3. Results and Discussion

Fig.6-7 shows the tensile testing results for the single-material coupons. PLA exhibits higher strength and elastic modulus but also more brittle behaviors compared to PETg. From Fig.6, it could also be seen that the large elongation to failure of the PETg component (Fig.7) is primarily attributed to the stretching of the fibrils. Considering the fact that with material extrusion process the fibrils are defined essentially by the individually deposited tracks, it could also be hypothesized that the process setting for PETg might not be well-tuned in this study, which resulted in relatively low inter-track bonding and consequently failure mode dominated by inter-track delamination. As it is not within the interest of this study to investigate the failure mode of material extrusion constructions, this was not further investigated. Instead, the baseline material properties were utilized for subsequent experimental discussions (**Table 3**).



a. PLA



b. PETg

Fig.6 Single-material tensile coupons after testing

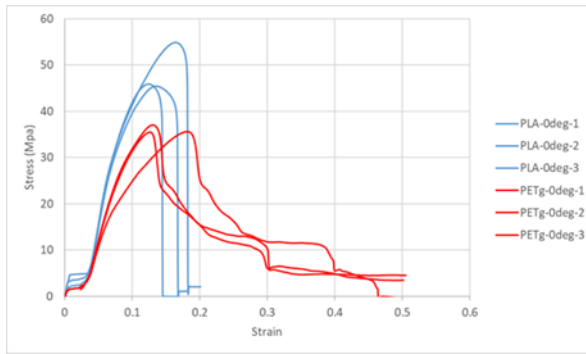


Fig.7 Stress-strain curves of PLA and PETg coupons

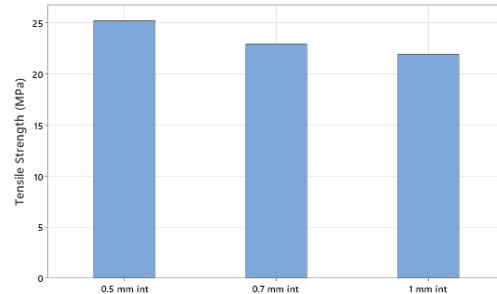
Material	Yield strength (MPa)	Max. strength (MPa)	Elastic modulus (MPa)	Ductility (%)
PLA	17.65513	48.76509	823.9766667	17.65513
PETg	11.80584333	36.03926336	553.6733333	35.89736667

Table 3: Mechanical properties baselines of PLA and PETg

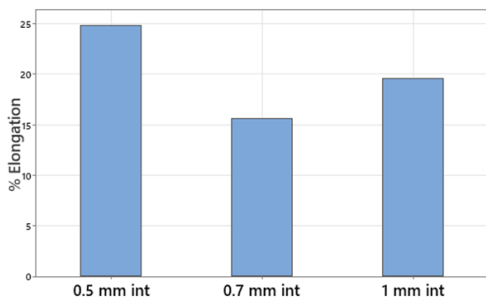
The tensile testing results for the benchmark interface samples are presented in **Fig.8**, and a representative sample after failure is illustrated in **Fig.9**. All the benchmark interface samples failed along the PLA-PETg interface, demonstrating low intrinsic material compatibility. The artificially introduced overlap in the model did facilitate more significant bonding with the interface, although this effect does not appear to scale with the overlapping size. In addition, although not inspected, it could be expected that the overlap design would result in loss of dimensional accuracy and possibly feature resolution for small-size features for applications.



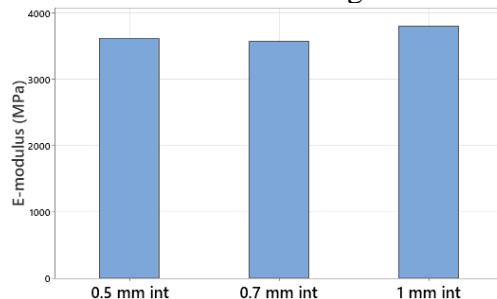
a. Stress-strain curve



b. Ultimate strength



c. Elongation to breakage



d. Elastic modulus

Fig.8 Mechanical properties of the benchmark material interface



Fig 9: All benchmark interface samples fractured along PLA-PETG interface (showing 0.7mm-overlap interface)

For the tensile testing of the cellular interface samples, the failure is located on the PETg side of the end of the cellular interface section for all the samples, as illustrated in Fig.10 for the Aux-60RD-PETg sample. Fig.11-13 shows the stress-strain curves of the cellular interface samples with PLA for the positive component and re-entrant auxetic, octahedral and BCC designs, respectively. It is noted that due to the non-standard gripping end geometry designs and the occurrence of defects with the gripping ends that could be found with some samples, the initial sections of the stress-strain curves for many of the interface samples do not reflect the tension of the sample but instead the slacking of the setup. Therefore, the curves were treated with extra care during analysis of mechanical properties.

For the re-entrant auxetic-based design, the behaviors of individual samples exhibit some non-consistency, which might be caused by both process defects and the unit cell topology design. The re-entrant auxetic unit cell contains vertical elements of relatively small thickness (1.3mm), which could potentially cause reduced process quality and large property variability. There exists a significant change of mechanical strength with the increase of cellular design relative density from 0.4 to 0.5, and comparatively less change between relative densities 0.5 to 0.6. Further inspection with the fracture surface reveals that this was likely attributed to the change of the fracture mode. For the Aux-40RD-PLA samples, the fracture surfaces exhibit relative smooth and planar tomography (Fig.15), indicating relative comparative significances of both the PLA and the PETg phases during fracture failure. On the other hand, for the Aux-50-RD-PLA and Aux-60-RD-PLA samples, fractured tracks that are partially pulled loose from the main structure are clearly present on the fracture surfaces, and the overall surface tomography exhibits more obvious topology-influenced pattern (Fig.14 and Fig 16). This might be due to the reduced volume (are consequently areal) percentage of the relatively weaker PETg phase at 0.5 and 0.6 relative densities, which resulted in PETg-phase-dominated failure with the samples.

In comparison, the stress-strain curves of the octahedral-based and BCC-based cellular interfaces are relatively consistent. The octahedral designs exhibit a somewhat more “brittle” behavior, with residual strength of the interface rapidly decreasing with additional strain. On the other hand, the BCC designs exhibit higher strength and higher overall ductility, which can be clearly discerned from the long tails of the stress-strain curves (Fig.13) that indicate high residual strength after initial failure. The failure characteristics of both types of interfaces exhibit significant influence from the weaker PETg phase. The fracture surfaces exhibit both PETg phase pull-out and loose PETg tracks (Fig.14 and Fig.16), which indicate that not only does the PETg negative components

are more significantly loaded, but also that the inter-track bonding of the PETg phase becomes a significant cause of failure.

The effects of relative density of cellular structure on the interface property are significant for both types of cellular interface designs, although the trends are different. For the octahedral designs, the increase of relative density of cellular design resulted in a decrease of strength, whereas the opposite trend was observed for the BCC designs. As PLA exhibits higher mechanical strength, it is intuitive that an optimal material composition for the highest interfacial strength would consist of larger percentage of PETg and smaller percentage of PLA. However, for the BCC designs, such rather simplistic design approach does not appear to hold valid. Another observation was that the BCC-based interfaces exhibit the highest overall strength among the three designs (Fig.17). For stand-alone cellular structures, BCC typically exhibits relatively low strength, especially when compared to a stretch-dominated design (e.g. octahedral). Therefore, it could be reasonably concluded that the classic design rules of cellular structures are significant to the design of cellular interfaces, however the actual influences could be very different.



Fig.10 Fractured Aux-60RD-PETg

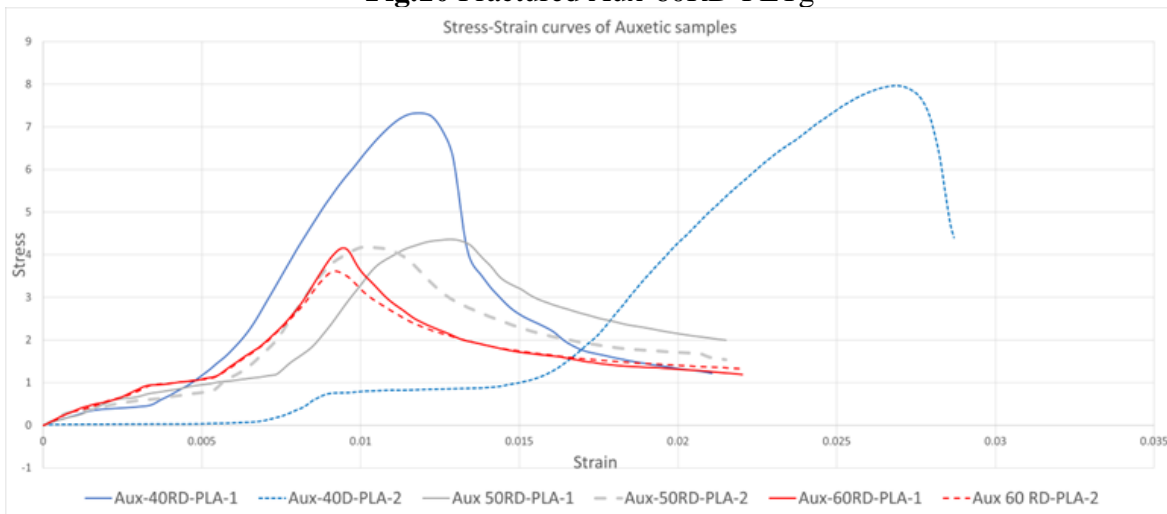


Fig.11 Stress-strain curves for re-entrant auxetic cellular interface samples

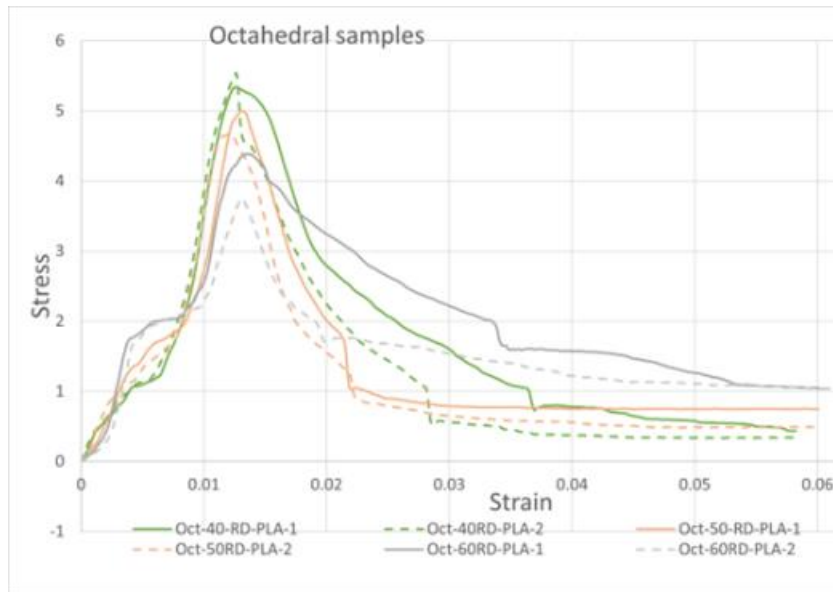


Fig.12 Stress-strain curves for octahedral cellular interface samples

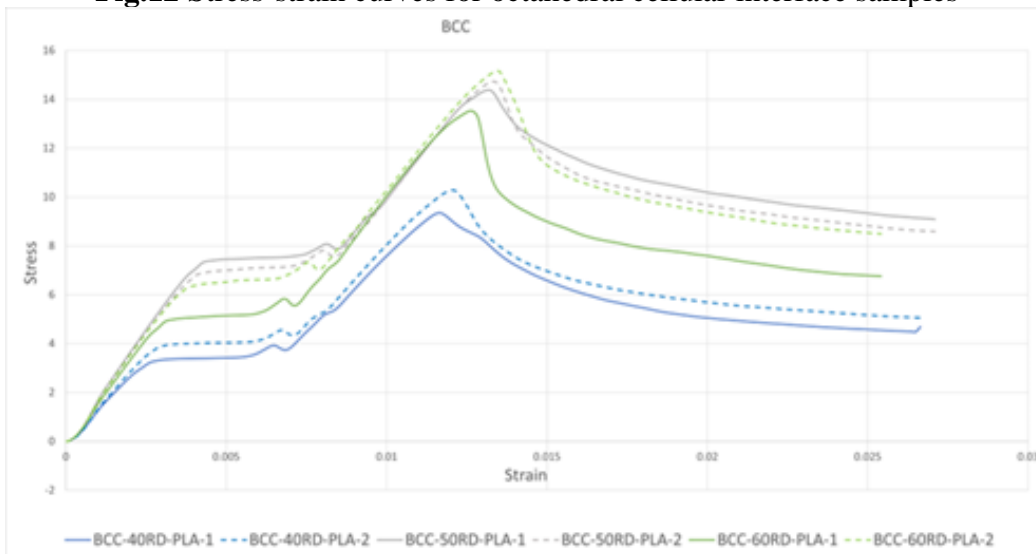
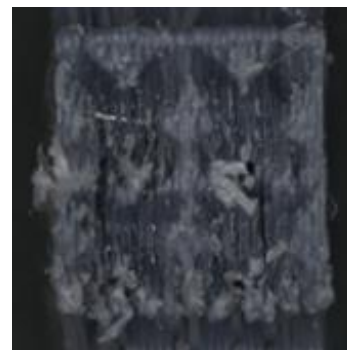


Fig.13 Stress-strain curves for BCC cellular interface samples



a. View into the PLA side



b. View into the PETg side

Fig.14 Fracture surface of Oct-40RD-PLA



a. View into the PLA side



b. View into the PETg side

Fig.15 Fracture surface of Aux-40RD-PLA

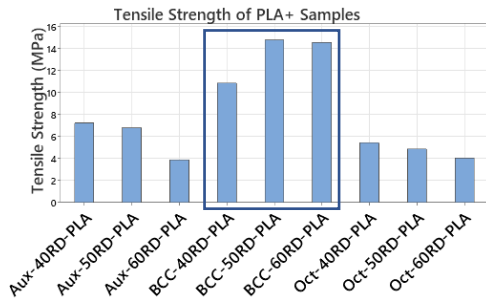


a. View into the PLA side

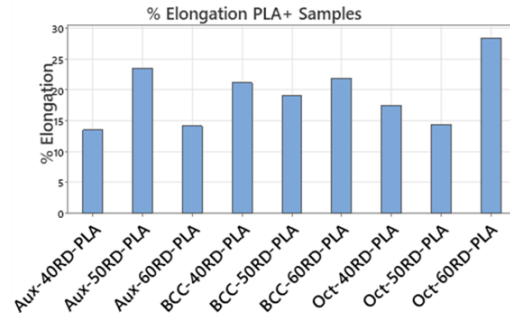


b. View into the PETg side

Fig.16 Fracture surface of Aux-50RD-PLA



a. Tensile strength



b. Elongation at break

Fig 17: Tensile properties of cellular interfaces with PLA positive components

When the material assignment flipped, the different interface designs exhibit significant change of behaviors. As shown in Fig.18-20, the stress-strain curves of all three cellular interface designs with PETg positive components exhibit completely different characteristics compared to those with PLA positive components.

For the re-entrant auxetic design (Fig.18), the effect of relative density on maximum strength become less significant, while the behaviors of samples for the same design become more consistent. This was found to be mainly attributed to the more consistent failure mechanism with these structures, which is dominated by the weaker PETg phase. With the PETg positive components, the cellular strut features become the critical features of the interface structures, which upon failure exhibit both fracture and pull-out behaviors. In addition, the quality of the PLA

negative component also appears to be lower compared to the counterparts with PLA as the material of the positive components. This was hypothesized to be caused by the setting with the process parameters but was not further investigated. On the other hand, the stress-strain behaviors of the octahedral designs (Fig.19) become more scattered. It was also found that the fracture surfaces of the octahedral samples exhibit relative smooth tomography. The consistency of the relationship between the increased variability of the stress-strain curves with the cellular interfaces and the fracture surface smoothness suggests a potential general design guideline for such interfaces that with increased efficiency of the design of the two component phases, the variability of the resulting structures also become less consistent due to the non-negligible effects of multiple failure mechanisms. Lastly, the effect of relative density design on the overall performance of the BCC interface appears less significant compared to be less significant compared to the other cellular topology designs as well as the counterpart structures with the PLA positive components (Fig.20). Additional information about the mechanical properties of the three interfaces with PETg positive components is shown in Fig.21.

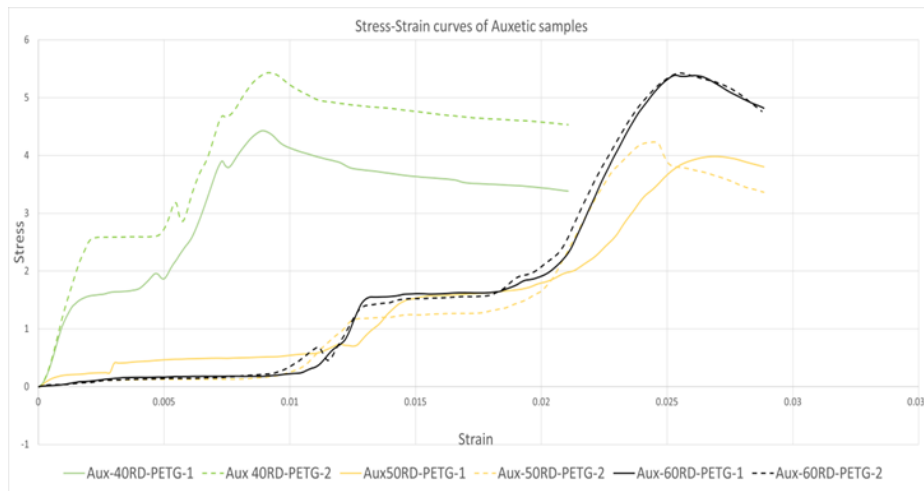


Fig.18 Stress-strain curve of re-entrant auxetic interface with PETg positive component

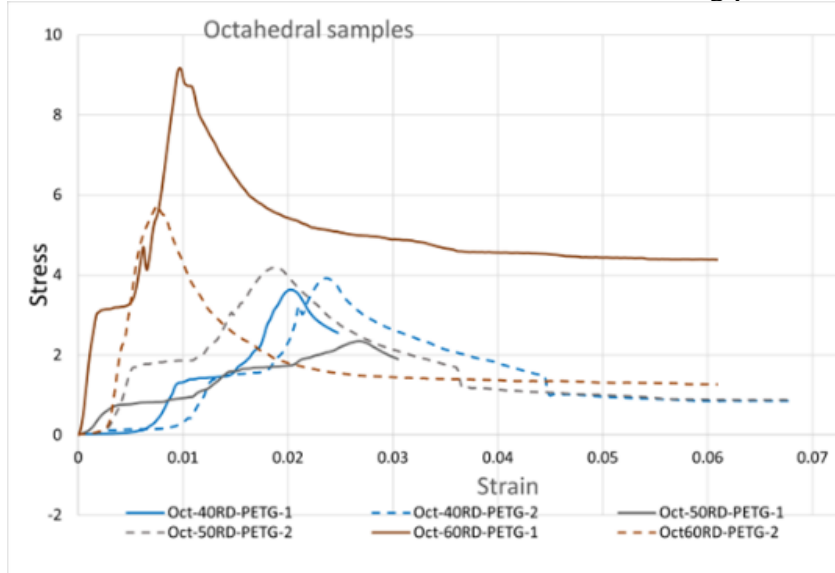


Fig.19 Stress-strain curve of octahedral interface with PETg positive component

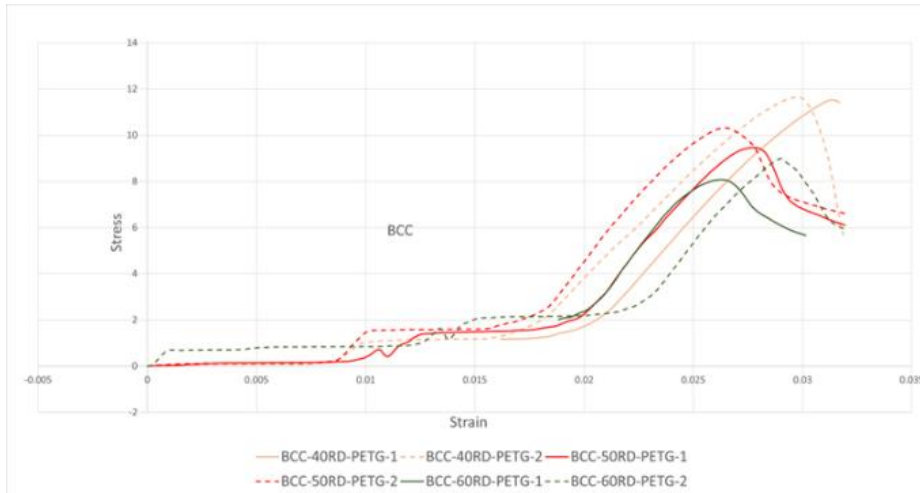
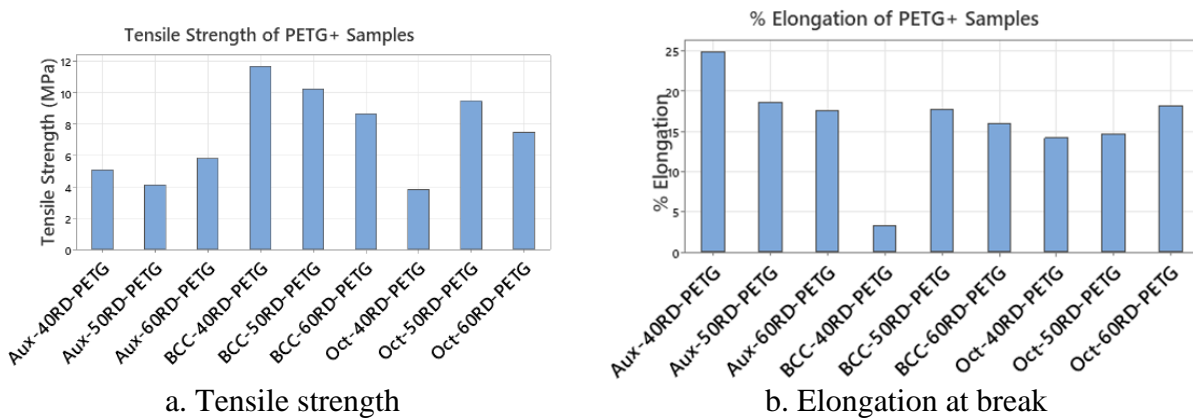


Fig.20 Stress-strain curve of BCC interface with PETg positive component



a. Tensile strength

b. Elongation at break

Fig.21: Tensile testing results of PETG+ samples

An additional FEA analysis was carried out with the three types of interfaces at varying levels of cellular relative density designs. The FEA analysis was set up using perfectly-elastic materials using the elastic modulus obtained from experimentation. Without the consideration of plasticity within the materials, it was not expected that the FEA provides accurate estimation of the behaviors of the structures. However, even for elastic modulus estimation the FEA results differed from the experimentation. As shown in Fig.22, the re-entrant auxetic interface was predicted to exhibit the highest overall elastic modulus at all relative density levels. Such discrepancy is again likely attributed to the processing-induced issues, as the material extrusion systems used for this study consistently appeared to exhibit quality consistency issues with the cellular interface structures, possibly due to the frequent switching of active material extrusion printheads. This remains a topic for further investigation.

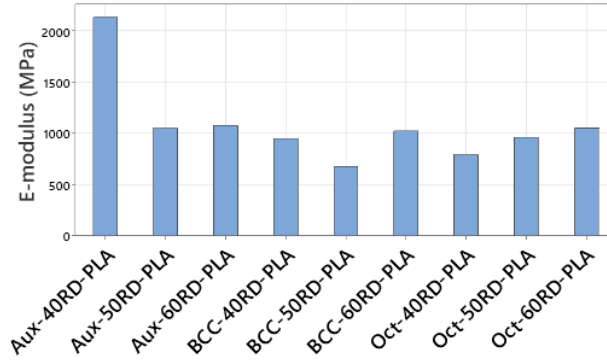


Fig.22 Elastic modulus of cellular interface samples with PETg positive components

4. Conclusion

The current study investigated a new bi-material interface design concept based on cellular structures. Overall, the cellular design-based interface exhibit significantly improved overall ductility and mechanical property controllability. The unit cell topology of the cellular structures exhibit significant effects on the behaviors and properties of the cellular interfaces, which could potentially be exploited for property control with these designs. In addition, the design of the interface cellular structures appears to be influence by the mechanical properties of the two component materials. Finally, the behaviors of the cellular interfaces appear to differ from the classic knowledge with cellular structure designs, although some of the design rules with cellular unit cell still appear to be significant with the interface designs.

5. Acknowledgement

The authors would acknowledge the support of experimental resources from Additive Manufacturing Institute of Science and Technology (AMIST) Center at University of Louisville.

Reference

- [1] A. Bandyopadhyay and B. Heer, "Additive manufacturing of multi-material structures," *Materials Science and Engineering: R: Reports*, vol. 129, pp. 1-16, 2018.
- [2] H. Watschke, L. Waalkes, C. Schumacher, and T. Vietor, "Development of novel test specimens for characterization of multi-material parts manufactured by material extrusion," *Applied Sciences*, vol. 8, no. 8, p. 1220, 2018.
- [3] C. Yang, X. Tian, T. Liu, Y. Cao, and D. Li, "3D printing for continuous fiber reinforced thermoplastic composites: mechanism and performance," *Rapid Prototyping Journal*, vol. 23, no. 1, pp. 209-215, 2017.
- [4] M. A. H. Khondoker, A. Asad, and D. Sameoto, "Printing with mechanically interlocked extrudates using a custom bi-extruder for fused deposition modelling," *Rapid Prototyping Journal*, vol. 24, no. 6, pp. 921-934, 2018.
- [5] R. Freund, H. Watschke, J. Heubach, and T. Vietor, "Determination of influencing factors on interface strength of additively manufactured multi-material parts by material extrusion," *Applied Sciences*, vol. 9, no. 9, p. 1782, 2019.
- [6] L. Lopes, A. Silva, and O. Carneiro, "Multi-material 3D printing: The relevance of materials affinity on the boundary interface performance," *Additive Manufacturing*, vol. 23, pp. 45-52, 2018.

- [7] S. Zhao, F. Kimura, S. Kadoya, and Y. Kajihara, "Experimental analysis on mechanical interlocking of metal–polymer direct joining," *Precision Engineering*, vol. 61, pp. 120-125, 2020.
- [8] L. Rossing, R. B. Scharff, B. Chömpff, C. C. Wang, and E. L. Doubrovski, "Bonding between silicones and thermoplastics using 3D printed mechanical interlocking," *Materials & Design*, vol. 186, p. 108254, 2020.
- [9] T. Perets, N. B. Ghedalia-Peled, R. Vago, J. Goldman, A. Shirizly, and E. Aghion, "In vitro behavior of bioactive hybrid implant composed of additively manufactured titanium alloy lattice infiltrated with Mg-based alloy," *Materials Science and Engineering: C*, vol. 129, p. 112418, 2021.
- [10] S. Verma, C.-K. Yang, C.-H. Lin, and J. Y. Jeng, "Additive manufacturing of lattice structures for high strength mechanical interlocking of metal and resin during injection molding," *Additive Manufacturing*, p. 102463, 2021.
- [11] L. Yang, A. Coriano. A comparative study with the topology design of cellular mechanical interface in a bi-material structure. Presentation. International Solid Freeform Fabrication Symposium, Austin, TX, 2021.